Available online at www.sciencedirect.com
SCIENCE DIRECT®
International Journal of Heat and Mass Transfer 49 (2006) 4482–4495
International Journal of HEAT and MASS TRANSFER
www.elsevier.com/locate/ijhmt

Directional radiative properties of anisotropic rough silicon and gold surfaces

H.J. Lee, Y.B. Chen, Z.M. Zhang *

George W. Woodruff School of Mechanical Engineering, Georgia Institute of Technology, Atlanta, GA 30332, USA

Received 26 September 2005
Available online 25 July 2006

Abstract

Recent studies have shown that the topography of some chemically etched microrough silicon surfaces is non-Gaussian and may be strongly anisotropic. However, the bidirectional reflectance distribution function (BRDF) of anisotropic surfaces has not been fully understood. The present study uses the Monte Carlo method to investigate the out-of-plane BRDF, multiple scattering, and the change of the polarization state upon reflection. Two ray-tracing algorithms are developed that incorporate the surface topography or slope distribution of the samples obtained by the use of an atomic force microscope. The predicted BRDFs for silicon surfaces with or without a gold coating are in reasonable agreement with the results measured using a laser scatterometer at a wavelength of 635 nm. The employment of surface topographic data is indispensable to the BRDF modeling of anisotropic surfaces. While first-order scattering makes the dominant contribution to reflections from the studied surfaces, it is critical to consider the polarization state change in order to correctly predict the out-of-plane BRDF. The versatile Monte Carlo modeling tools developed through the present study help gain a better understanding of the directional radiative properties of microrough surfaces and, furthermore, will have an impact on thermal metrology in the semiconductor industry.

Keywords: Bidirectional reflectance; Monte Carlo method; Radiative properties; Surface roughness

1. Introduction

Understanding the radiative properties of semiconductors is essential for the advancement of manufacturing technology, such as rapid thermal processing for annealing and chemical vapor deposition [1]. Because the major heating source in rapid thermal processing is lamp radiation, knowledge of radiative properties is important for the thermal budget and temperature control during the process. A challenging problem is the accurate measurement of wafer temperature based on radiation thermometry, which is preferred because of its non-intrusiveness and fast response [2,3]. The accuracy of radiation thermometry can be affected by emittance changes and background radiation, especially when a surface is rough, such as the backside of silicon wafers. Surface roughness affects not only the emittance of a wafer but also the directional distribution of the reflected radiation by scattering [4–6]. The emittance of a rough surface can be simply obtained from directional radiative properties, based on Kirchhoff's law and the conservation of energy [6–8]. Furthermore, knowledge of directional radiative properties allows modeling of radiative heat transfer between rough surfaces and thereby modeling of an effective emittance with the consideration of background radiation [9,10]. Therefore, a detailed understanding of the directional radiative properties associated with scattering from rough surfaces is essential for temperature measurements in rapid thermal processing.

The bidirectional reflectance distribution function (BRDF) describes spatial distribution of light scattered from rough surfaces and can be used to calculate other radiative properties. Rigorous approaches to predict the

* Corresponding author. Tel.: +1 404 385 4225; fax: +1 404 894 8496.
E-mail address: zhuomin.zhang@me.gatech.edu (Z.M. Zhang).

0017-9310/$ - see front matter © 2006 Elsevier Ltd. All rights reserved.
doi:10.1016/j.ijheatmasstransfer.2006.05.022

Nomenclature

f_r	bidirectional reflectance distribution function, sr^{-1}
G	energy of ray bundles
h	unit vector perpendicular to the plane of incidence or reflection
r	Fresnel's reflection coefficient
s	unit vector in the direction of incidence or reflection
v	unit vector parallel to the plane of incidence or reflection
w	root-mean-square slope

Greek symbols

ζ_x	microfacet slope in x-direction
ζ_y	microfacet slope in y-direction
θ	zenith angle, deg
λ	wavelength in vacuum, m
ρ	microfacet reflectivity
σ	root-mean-square roughness, m
τ	autocorrelation length, m
ϕ	azimuthal angle, deg
ω	solid angle, sr

Subscripts

i	incidence
p	p-polarization (TM wave)
r	reflection
s	s-polarization (TE wave)

BRDF of rough surfaces usually involve the numerical solution of Maxwell's equations, considering the surface topography and the dielectric properties of materials [11,12]. Because of the complexity of electromagnetic theory, however, a number of approximate techniques such as perturbation theory, the Kirchhoff approximation, and the geometric optics approximation (GOA) have been widely used [13–15]. GOA assumes that effects of interference and diffraction are negligible and a surface is composed of numerous microfacets where an incident ray reflects specularly. Under these assumptions, ray-tracing techniques can be applied to predict the BRDF either with the appropriate analytical expression [16–19] or with the Monte Carlo method [20–23].

Most studies on light scattering assume that roughness is random and follows Gaussian statistics [11–23]. However, this assumption breaks down for many natural or engineered surfaces, which reveal non-Gaussian and anisotropic statistics [24–28]. Zhu and Zhang [27,28] demonstrated that the slope distribution function (SDF) of several microrough silicon surfaces is non-Gaussian and highly anisotropic, even though the height distribution is close to a Gaussian function. The non-Gaussian and anisotropic features may be attributed to chemical etching, which is a common process to remove surface defects. Due to limitations of the analytical approach, only in-plane BRDFs with first-order scattering were considered in the works of Zhu and Zhang [27,28].

In the present work, the BRDF of anisotropic surfaces is modeled using Monte Carlo ray-tracing methods. The decomposition of polarization upon reflection by the randomly oriented microfacets of a two-dimensional (2-D) surface is taken into account. Two ray-tracing algorithms are developed to implant the measured surface topographic data from an atomic force microscope (AFM): one based on the surface topography and the other based on the SDF. The applicability of the Monte Carlo method is verified by comparison with the BRDF measured with a laser scatterometer [29]. Furthermore, by depositing a gold film onto the rough silicon surfaces using an e-beam evaporator, the study of light scattering by non-Gaussian and anisotropic surfaces is extended to metallic surfaces.

2. Monte Carlo ray-tracing methods

Based on GOA, the BRDF can be predicted with analytical models or Monte Carlo ray-tracing methods. Analytical models of GOA are usually reduced from the Kirchhoff approximation in a short wavelength limit [13–15] while some models are derived from statistical ray tracing [16,17]. An analytical model of the BRDF is proportional to the SDF and the reflectivity of a material. The use of an analytical formula allows the convenient calculation of the BRDF without a lengthy numerical procedure as required by the Monte Carlo method. However, most analytical models deal with first-order scattering only. Although some analytical expressions have incorporated multiple scattering, additional assumptions must be made and the model cannot fully capture the characteristics of multiple scattering [16,17]. Multiple scattering becomes significant for surfaces with large slopes or for large angles of incidence or reflection. On the other hand, in the Monte Carlo method, a large number of rays are illuminated on a rough surface and traced numerically until they leave the surface [20–23]. Numerical ray tracing with the Monte Carlo method allows the complete treatment of multiple scattering. The propagating direction of each ray is determined from the specular reflection at a microfacet, and its energy is reduced by the reflectivity obtained from Fresnel's reflection coefficient. The BRDF is obtained from a ratio between the energy of rays reflected into a given solid angle and the energy of all incoming rays.

Distinguished by how to simulate rough surfaces, two ray-tracing techniques can be applied for modeling the

BRDF using the Monte Carlo method: the surface generation method (SGM) [20,21] and the microfacet slope method (MSM) [22,23]. SGM is the most commonly used ray-tracing method, in which a surface realization (i.e., a numerically generated rough surface) is required prior to tracing the ray bundles. A surface realization provides a discrete surface profile, from which all statistical descriptions of a rough surface can be calculated. Therefore, the origin and direction of reflection is determined based on the physical location and orientation of the microfacet that the ray strikes. BRDF is obtained from an ensemble average over a sufficiently large number of surface realizations. On the other hand, MSM takes advantage of a basic concept of GOA; for an incident ray, only the normal vector of a microfacet determines the reflection direction of rays and the reflectivity according to Fresnel's formula. The numerical generation of a rough surface profile is not necessary; rather, the orientation of a microfacet is generated for each incoming ray. The generation of the normal vector of a microfacet is based on the SDF and the direction of an incoming ray [23]. Because a surface profile does not exist in MSM, the optical path of a propagating ray and whether the ray re-strikes the surface cannot be directly determined. Hence, MSM relies on a shadowing function, which is the probability that a reflected ray re-strikes another surface facet, to model multiple scattering. The use of the shadowing function imposes a limitation of the MSM, such that it cannot be applied for very rough surfaces at oblique incidence or large reflection angles [30]. In addition, the shadowing function is not available for anisotropic surfaces and the adoption of a shadowing function to an anisotropic surface introduces further approximation. The advantage of MSM is that it takes less computational time than SGM and can be applied to multiscale problems, such as light scattering from semitransparent materials [22,23]. More detailed discussion and intercomparison of the two ray-tracing algorithms can be found in the previous publications [21,23,30].

A common method for surface realizations in SGM is to use a power spectrum, known as the spectral method [14,31,32]. The power spectrum contains information for both vertical and lateral scales of roughness in the Fourier space, and its inverse Fourier transform yields a surface profile. The power spectrum and the autocovariance function, which is the autocorrelation function multiplied by a variance σ^2, are a Fourier transform pair. Therefore, a rough surface, defined by an autocorrelation function and a root-mean-square (rms) roughness, is usually generated with the spectral method, regardless of whether the autocorrelation function is Gaussian or not [31]. If the Gaussian autocorrelation function is used, that surface realization is simply referred to as a Gaussian surface. Even though the power spectrum of anisotropic silicon wafers used in the present study can be obtained from surface topography measured with an AFM [33], it is not feasible to generate an anisotropic surface with this method. Knotts et al. [34] fabricated 1-D randomly rough surfaces to compare theory and experiment in light scattering. They measured the topography of the fabricated surfaces with a stylus profilometer and showed that the measured surface statistics are not consistent with Gaussian statistics in higher-order probability densities. They found that the prediction for 1-D rough surfaces based on the direct use of the topographic measurements yields much better agreement with experiment. In the present study, the method of direct implementation is extended to the study of 2-D rough surfaces. The surface topographic data from the AFM measurement were stored in a 2-D array of surface height, which can be conveniently incorporated into the SGM algorithm.

In MSM, unique information on roughness is taken from the SDF to determine the orientation of microfacets. The SDF of anisotropic surfaces can be numerically evaluated as a 2-D histogram using topographic data [27]. A weight function must be included in generating the normal vector of a microfacet because, statistically, the incident energy that is intercepted by the microfacet depends not only on the SDF but also on the projected area of the microfacet. Lee et al. [23] used the rejection method to generate the normal vector of microfacets following a weighted SDF with uniform random numbers. Because the rejection method is suitable for any type of distribution function as long as a comparison function is appropriately selected [35], the algorithm developed by Lee et al. [23] is also applicable for the SDF of anisotropic surfaces with a new comparison function. Using a Gaussian functional form, new comparison functions are selected to be always greater than the SDF by adjusting both an rms value of the Gaussian function and a multiplying constant. Meanwhile, the Smith shadowing function [36] determines the probability of re-striking in MSM, and it requires the ratio of rms roughness σ to autocorrelation length τ as an input. For Gaussian surfaces, the rms slope w is equal to $\sqrt{2}\sigma/\tau$ [13,14]. This relation ensures that SGM and MSM yield the same results in the regime where MSM is valid [30]. However, the surfaces used in the present study do not obey this relation. The difference between SGM and MSM for anisotropic surfaces will be further examined.

Most published works on the use of the Monte Carlo method in predicting BRDFs and calculating the radiative heat transfer between rough surfaces do not consider the polarization effect [5,20–23,37–39]. However, the polarization state generally changes upon reflection by a 2-D rough surface because of the random orientation of microfacets [13–15]. As a result, the polarization of the scattered wave is different from that of the incident wave, i.e., depolarization occurs. In a different type of ray-tracing method, the amplitude of the electric field is traced, considering both phase and polarization rather than the intensity of rays [40]. This method is beyond the domain of GOA and requires a normalization to observe energy conservation. Therefore, the present study extends the Monte Carlo method based on GOA to modeling the BRDF by taking into account the change of the polarization state in the ray-tracing algorithm. The microfacet reflectivity is

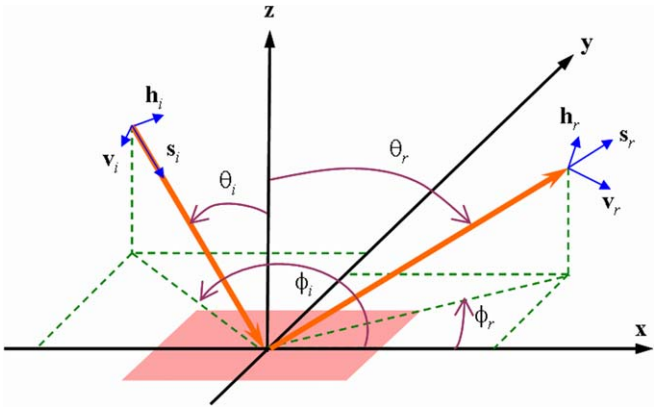

Fig. 1. Schematic of incident and scattered waves. Here, x, y, and z are the global coordinates, where the x–y plane is the mean plane of a rough surface. θ_i and ϕ_i are the zenith and azimuthal angles of incidence, whereas θ_r and ϕ_r are the zenith and azimuthal angles of reflection, respectively. $\mathbf{s}_i$ and $\mathbf{s}_r$ are unit vectors in the direction of incidence and reflection, respectively. A unit vector $\mathbf{h}_i$ is perpendicular and a unit vector $\mathbf{v}_i$ is parallel to the plane of incidence, whereas unit vectors $\mathbf{h}_r$ and $\mathbf{v}_r$ are perpendicular and parallel to the plane of reflection, respectively.

calculated in the local coordinates using Fresnel's reflection coefficients, considering the change of the polarization state.

The incident light may be decomposed into two linear polarizations: s-polarization (TE wave) and p-polarization (TM wave). The electric field or the magnetic field is perpendicular to the plane of incidence for s-polarization or p-polarization, respectively. In a 2-D rough surface, even though the incident light is purely s- or p-polarized, both polarization components are present in the local coordinates of a microfacet. The geometrical relations between wave vectors and polarization vectors delineate the contribution of each polarization to the reflectivity. As illustrated in Fig. 1, unit vectors in the direction of incidence and reflection, $\mathbf{s}_i$ and $\mathbf{s}_r$, are defined with the zenith angles (θ_i and θ_r) and azimuthal angles (ϕ_i and ϕ_r) in the following manner:

$$\mathbf{s}_i = \begin{pmatrix} -\sin\theta_i\cos\phi_i \\ -\sin\theta_i\sin\phi_i \\ -\cos\theta_i \end{pmatrix}, \quad \mathbf{s}_r = \begin{pmatrix} \sin\theta_r\cos\phi_r \\ \sin\theta_r\sin\phi_r \\ \cos\theta_r \end{pmatrix} \tag{1}$$

In global coordinates, the vectors $\mathbf{s}_i$ and $\mathbf{z}$ define the plane of incidence, and the vectors $\mathbf{s}_r$ and $\mathbf{z}$ define the plane of reflection. A unit vector $\mathbf{h}_i$ perpendicular and a unit vector $\mathbf{v}_i$ parallel to the plane of incidence characterize the two polarizations of the incident wave. Here, $\mathbf{h}_i$ indicates the electric field for s-polarization and $\mathbf{v}_i$ for p-polarization. Similarly, unit vectors $\mathbf{h}_r$ and $\mathbf{v}_r$ represent the two polarizations of the reflected wave. Hence,

$$\mathbf{h}_i = \frac{\mathbf{z}\times\mathbf{s}_i}{|\mathbf{z}\times\mathbf{s}_i|} = \begin{pmatrix} \sin\phi_i \\ -\cos\phi_i \\ 0 \end{pmatrix}, \quad \mathbf{h}_r = \frac{\mathbf{z}\times\mathbf{s}_r}{|\mathbf{z}\times\mathbf{s}_r|} = \begin{pmatrix} -\sin\phi_r \\ \cos\phi_r \\ 0 \end{pmatrix} \tag{2}$$

$$\mathbf{v}_i = \mathbf{h}_i\times\mathbf{s}_i = \begin{pmatrix} \cos\theta_i\cos\phi_i \\ \cos\theta_i\sin\phi_i \\ -\sin\theta_i \end{pmatrix}, \quad \mathbf{v}_r = \mathbf{h}_r\times\mathbf{s}_r = \begin{pmatrix} \cos\theta_r\cos\phi_r \\ \cos\theta_r\sin\phi_r \\ -\sin\theta_r \end{pmatrix} \tag{3}$$

Calculation of the reflectivity involves two conversions of the polarization components. The s- and p-polarization components of incidence defined in the global coordinates are first converted to counterparts in the local coordinates. The local polarization components are multiplied by Fresnel's reflection coefficients, respectively, and then converted to the global components. Accordingly, the microfacet reflectivities for co-polarization and cross-polarization can be expressed as follows [18,19]

$$\rho_{ss} = |(\mathbf{v}_r\cdot\mathbf{s}_i)(\mathbf{v}_i\cdot\mathbf{s}_r)r_s + (\mathbf{h}_r\cdot\mathbf{s}_i)(\mathbf{h}_i\cdot\mathbf{s}_r)r_p|^2/|\mathbf{s}_i\times\mathbf{s}_r|^4 \tag{4a}$$

$$\rho_{sp} = |(\mathbf{h}_r\cdot\mathbf{s}_i)(\mathbf{v}_i\cdot\mathbf{s}_r)r_s - (\mathbf{v}_r\cdot\mathbf{s}_i)(\mathbf{h}_i\cdot\mathbf{s}_r)r_p|^2/|\mathbf{s}_i\times\mathbf{s}_r|^4 \tag{4b}$$

$$\rho_{ps} = |(\mathbf{v}_r\cdot\mathbf{s}_i)(\mathbf{h}_i\cdot\mathbf{s}_r)r_s - (\mathbf{h}_r\cdot\mathbf{s}_i)(\mathbf{v}_i\cdot\mathbf{s}_r)r_p|^2/|\mathbf{s}_i\times\mathbf{s}_r|^4 \tag{4c}$$

$$\rho_{pp} = |(\mathbf{h}_r\cdot\mathbf{s}_i)(\mathbf{h}_i\cdot\mathbf{s}_r)r_s + (\mathbf{v}_r\cdot\mathbf{s}_i)(\mathbf{v}_i\cdot\mathbf{s}_r)r_p|^2/|\mathbf{s}_i\times\mathbf{s}_r|^4 \tag{4d}$$

where r denotes complex Fresnel's reflection coefficient for a given polarization. In the microfacet reflectivities, subscripts s and p stand for each polarization while the first and second subscripts stand for the incidence and the reflection, respectively.

In terms of the microfacet reflectivities, the reflected energies $G_{r,s}$ and $G_{r,p}$ are related to the incident energies $G_{i,s}$ and $G_{i,p}$ by

$$\begin{bmatrix} G_{r,s} \\ G_{r,p} \end{bmatrix} = \begin{bmatrix} \rho_{ss} & \rho_{ps} \\ \rho_{sp} & \rho_{pp} \end{bmatrix} \begin{bmatrix} G_{i,s} \\ G_{i,p} \end{bmatrix} \tag{5}$$

The reflectivity, defined as a ratio of the reflected energy, $G_r = G_{r,s} + G_{r,p}$, to the incident energy, $G_i = G_{i,s} + G_{i,p}$, depends on the incident polarization state. To facilitate calculation, the incident energy of each ray is set to unity such that $(G_{i,s}, G_{i,p}) = (1,0)$ for s-polarization, $(G_{i,s}, G_{i,p}) = (0,1)$ for p-polarization, and $(G_{i,s}, G_{i,p}) = (0.5, 0.5)$ for random polarization (i.e., unpolarized incidence). For the first reflection, $G_{r,s}$ and $G_{r,p}$ are calculated from Eq. (5). For multiple reflections, the previously reflected energies are substituted for $G_{i,s}$ and $G_{i,p}$, and the next reflected energy is updated according to Eq. (5). Each ray is traced until it leaves the surface, and then the information on its direction and energy for each polarization is stored in a database.

In a special case where the planes of incidence and reflection are identical, the polarization state is maintained for either s- or p-polarization if only first-order scattering is involved. Therefore, the vectors $\mathbf{h}_i$ and $\mathbf{h}_r$ are parallel or antiparallel (refer to Fig. 1); consequently, $\mathbf{h}_i\cdot\mathbf{s}_r = 0$ and $\mathbf{h}_r\cdot\mathbf{s}_i = 0$. From Eq. (4), ρ_{sp} and ρ_{ps} vanish, while $\rho_{ss} = |r_s|^2$ and $\rho_{pp} = |r_p|^2$. The corresponding BRDF is called the in-plane BRDF ($\phi_r = \phi_i$ or $\phi_r = \phi_i + 180°$). The cross-polarization term is non-zero even for in-plane BRDF when multiple scattering occurs.

After a large number of ray bundles are traced, the BRDF can be calculated in terms of the energies of the ray bundles [6]:

$$f_r(\lambda,\theta_i,\phi_i;\theta_r,\phi_r) = \frac{1}{G_i(\theta_i,\phi_i)}\frac{\Delta G_r(\theta_r,\phi_r)}{\cos\theta_r\Delta\omega_r} \tag{6}$$

where $G_i(\theta_i, \phi_i)$ is the total energy of the incident ray bundles and $\Delta G_r(\theta_r, \phi_r)$ is the energy of ray bundles leaving the surface within the solid angle $\Delta\omega_r$ in the direction (θ_r, ϕ_r). The integration of the BRDF yields the directional-hemispherical reflectance. The directional emittance can be obtained according to the conservation of energy and Kirchhoff's law [6]. Knowledge of the BRDF enables the calculation of the emittance of a rough surface and allows further study of the apparent or effective emittance of the surface considering the effect of surrounding radiation [5–10]. Note that the prediction of emittance via modeling the BRDF allows consideration of the effects of specific roughness statistics on emittance. Lee et al. [8] showed that the emittance of anisotropic wafers can be noticeably different from that of a Gaussian surface with the same rms roughness and autocorrelation length.

3. Surface characterization and BRDF instrumentation

Two silicon samples (Si-1 and Si-2) were selected from the wafers studied by Zhu and Zhang [28]. The wafers are lightly doped, 100 mm in diameter, and $\langle 100 \rangle$ single crystalline. Two gold samples (Au-1 and Au-2) were prepared by cutting Si-1 and Si-2 into $25 \times 25\ \text{mm}^2$ square pieces and depositing a gold film with an e-beam evaporator (CVC SC 5000) at the same time. A quartz crystal microbalance monitor displayed the thickness of a film during deposition within a relative uncertainty of 10%. A 20 nm thick titanium film was deposited directly onto the silicon substrate to prevent the gold film from peeling off. Next, a gold film with a thickness of 100 nm was deposited. The exact thickness is not important because the gold coating is thick enough to assume an opaque surface in the measurement and calculation of BRDFs.

The four samples were characterized with an AFM made by Digital Instruments (Dimension 3100 SPM). Zhu and Zhang [28] obtained the surface topography of the silicon wafers in the contact mode with silicon nitride tips, whose radius is less than 60 nm. In the contact mode, lateral or shear forces can distort surface features and reduce spatial resolution. Thus, deep valleys may not be correctly measured. This disadvantage resulted in spurious distributions for precipitous slopes [28]. In the present study, AFM scanning was performed in the tapping mode with sharper silicon tips, whose radius is less than 10 nm. At the expense of scanning speed, the AFM in the tapping mode with sharper tips allows measurement of precipitous slopes. The measured topographic data for a scanning area of $100 \times 100\ \mu\text{m}^2$ were stored in a 512×512 array. According to the instrument specifications, the uncertainty of the AFM measurement is estimated to be 3% both vertically and horizontally.

The surfaces of Si-1 and Si-2 were scanned five times each. The height distribution functions of the two samples look very similar to each other and resemble a Gaussian function although they have small negative values of skewness. The height distribution functions obtained in the present study are very similar to the previous work by Zhu and Zhang [28] and thus will not be presented. Because of its importance to the modeling, the SDF and its contour for Si-1 and Si-2 are plotted in Fig. 2. Both SDFs are non-Gaussian and anisotropic while the anisotropy of Si-1 is not as striking as that of Si-2. The SDF of Si-1 in Fig. 2a shows only one dominant peak at the center, indicating that a large number of microfacets are slightly tilted. The SDF of Si-2 also has a dominant peak at the center, though smaller than that of Si-1. Moreover, four large side peaks at $|\zeta_x| \approx |\zeta_y| \approx 0.36$, and three small side peaks at $|\zeta_x| \approx |\zeta_y| \approx 1.09$ appear in Fig. 2b. The contour plot clearly shows the three small side peaks although four of them are expected because of symmetry. Zhu and Zhang [28] demonstrated that the large and small side peaks are associated with the formation of $\{311\}$ and $\{111\}$ planes, respectively, during chemical etching in (100) crystalline wafers. Their measurement could not distinctly resolve the small side peaks due to the artifacts of the AFM, but the new measurement as shown in Fig. 2b clearly reveals three out of four small side peaks. The large and small side peaks in the SDF correspond to microfacets with inclination angles of 27.1° and 57.0°, respectively. However, the angles formed by $\{311\}$ and $\{111\}$ planes with respect to the (100) surface are, respectively, 25.2° and 54.7°, which are smaller than what the AFM measurements show. The large difference in the slopes cannot be explained by the 3% uncertainty in the AFM measurement, but may be caused by various artifacts, such as tip convolution. Depending on the size and shape of the tip compared to the curvature of surface roughness, tip convolution can cause the measured profile to be rougher or smoother than the actual topography, and these effects may exceed the specified uncertainty [41,42].

The rms roughness σ, the rms slope w, and the autocorrelation length τ are listed in Table 1, along with other pertinent parameters. For an anisotropic surface, w and τ vary with the azimuthal angle ϕ. However, based on the four-fold symmetry of Si-1 and Si-2, only the average values of w and τ over four representative directions, i.e., row $(\zeta_x = 0)$, column $(\zeta_y = 0)$, and two diagonals $(\zeta_x = \zeta_y$ and $\zeta_x = -\zeta_y)$ are presented. The difference in w or τ for row, column, and diagonal cases is almost negligible despite the anisotropic SDF of the two samples.

Since the gold samples were made by depositing thin films onto the silicon surfaces, it was expected that the SDF would not change much before and after the deposition. The topographic measurements of Au-1 and Au-2 were obtained with the same AFM two times each, and the average roughness statistics are listed in Table 1 for comparison. The SDFs of Au-1 and Au-2 (not presented) resemble those of Si-1 and Si-2 shown in Fig. 2, respectively. Although the calculated values of w of Au-1 and Au-2 are slightly greater than those of Si-1 and Si-2, they are within the standard deviation of AFM measurements of silicon samples. As a result, it is assumed that Si-1 and Au-1 or Si-2 and Au-2 have the same surface statistics

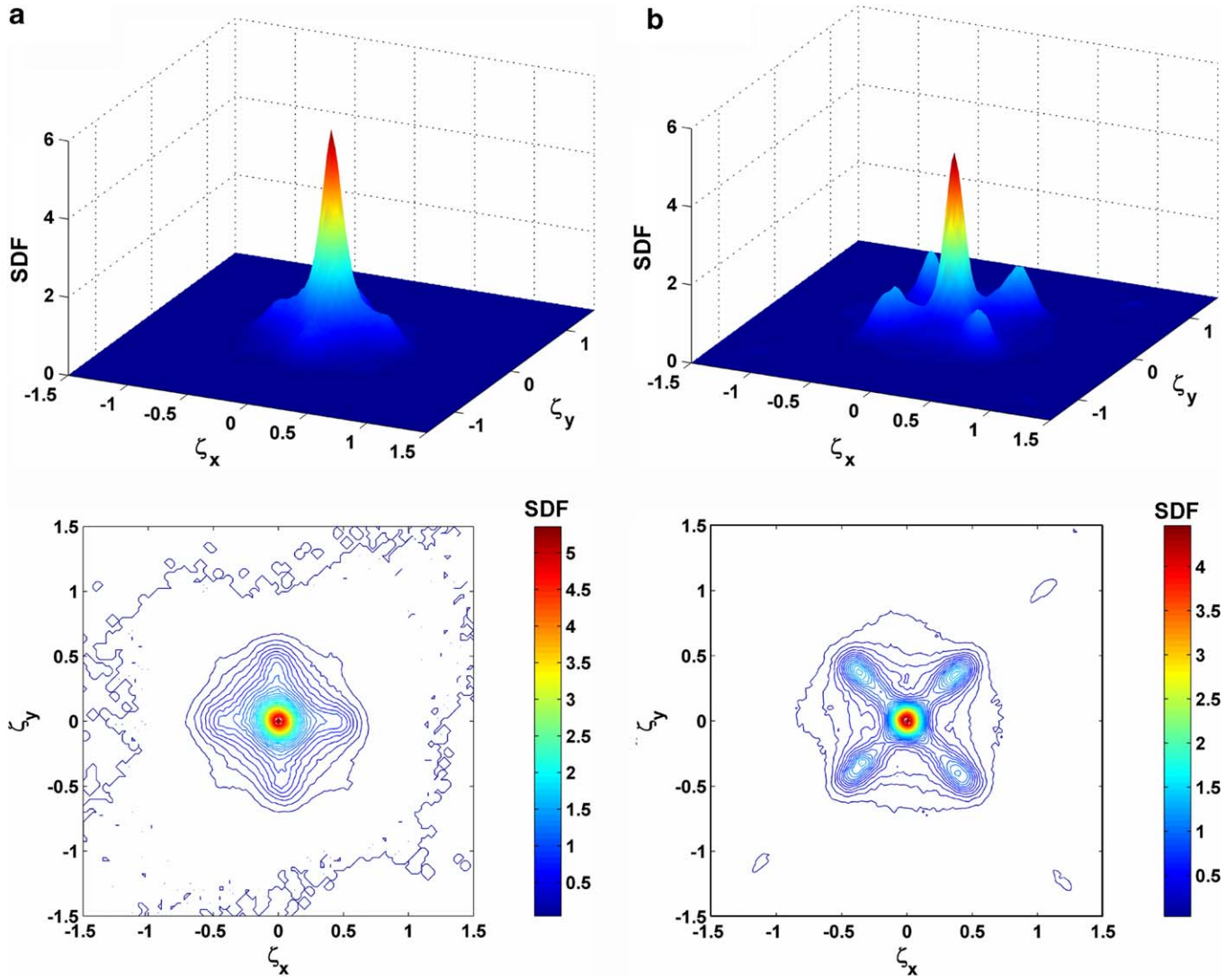

Fig. 2. 2-D slope distribution obtained from AFM measurements in 3-D plot (upper) and contour plot (lower). (a) Si-1; (b) Si-2.

Table 1
Sample description and roughness statistics

Sample	Si-1	Si-2	Au-1	Au-2
Crystalline orientation	⟨100⟩	⟨100⟩	N/A	N/A
Growth method	CZ	CZ	N/A	N/A
Doping type	P	P	N/A	N/A
Resistivity, Ω cm	4310–6970	10–40	N/A	N/A
Thickness, μm	525	500	0.1	0.1
σ, μm	0.51 ± 0.03	0.63 ± 0.04	0.50	0.65
w (along row/column)	0.28 ± 0.01	0.47 ± 0.04	0.29	0.50
w (along diagonals)	0.28 ± 0.01	0.47 ± 0.04	0.29	0.50
τ, μm (along row/column)	4.4 ± 0.4	3.1 ± 0.2	4.0	3.0
τ, μm (along diagonals)	4.3 ± 0.4	3.1 ± 0.2	3.9	3.1

despite the presence of the thin gold films. In the calculation of SGM, all seven sets of topographic data were used. Similarly, an averaged SDF based on the seven measurements was used in MSM. Because the shadowing function in MSM is developed for Gaussian surfaces, roughness parameters should be represented as one value. According to the seven topographic data sets, the rms roughnesses of Si-1 (or Au-1) and Si-2 (or Au-2) are 0.51 and 0.64, respectively. Similarly, after further averaging over the four representative directions for w and τ, $w = 0.28$ and $\tau = 4.2$ were used for Si-1 (or Au-1) and $w = 0.48$ and $\tau = 3.1$ for Si-2 (or Au-2).

The BRDF of the silicon wafers was measured with a laser scatterometer, specifically the three-axis automated scatterometer (TAAS) [29]. The TAAS is capable of measuring both the in-plane and out-of-plane BRDF. Three computer-controlled rotary stages change the zenith angle of incidence θ_i, zenith angle of reflection θ_r, and azimuthal angle of reflection ϕ_r. A manually controllable dial can vary the azimuthal angle of incidence ϕ_i. A semiconductor diode laser served as a coherent source for the measurement of BRDFs. A stationary detector measures the incident power while another movable detector measures the reflected power. Since the movable detector blocks illumination, the BRDF within $\pm 2.5°$ of the retroreflection direction ($\theta_r = \theta_i$ and $\phi_r = \phi_i$) cannot be measured with the

TAAS. The outputs of the two detectors are magnified by two pre-amplifiers and sent to a lock-in amplifier. The lock-in amplifier sends an oscillating current to a controller of the laser system and picks up the oscillating current from detected signals, thus eliminating the effect of background radiation in BRDF measurements. A computer controls the movement of the rotary stages and reads positions of those stages and outputs of the detectors. The half-cone angle of the solid angle subtended by the movable detector is approximately 0.5°, and thus a high angular resolution is achievable. Comparisons with a reference reflectometer at the National Institute of Standards and Technology indicate that the relative difference is within 5% [29].

4. Results and discussion

All the measured BRDFs are taken at a laser wavelength $\lambda = 635$ nm in the present study. The refractive indices of silicon and gold are $3.88 + 0.019i$ and $0.181 + 3.10i$, respectively, at this wavelength [43]. Therefore, the silicon wafers of approximately 500 μm thickness are opaque to the laser light. For the gold film, the thickness of 100 nm is much greater than the photon penetration depth of 16 nm. Although the local thickness of a film is reduced by the cosine of the microfacet inclination angle, it remains more than three times the penetration depth at an inclination angle of 60°. Furthermore, since the reflected radiation must travel through the gold film twice, the gold film can be safely regarded as semi-infinite in the measurement and calculation of BRDFs.

The angular resolution of $\Delta\theta$ and $\Delta\phi$ was set to 1° in the Monte Carlo method. A post-processing step smoothed the BRDF curves by averaging the values of nine adjacent nodes to reduce statistical noise in the calculations. The averaged SDF for the seven measurements is used in MSM. With twenty million ray bundles, MSM calculations result in a relative standard deviation less than 10% when the calculated values of $f_r \cos\theta_r$ are larger than 0.01. SGM calculations are performed on each of the seven topographic surfaces. A quarter million ray bundles are used for each surface, and BRDFs are averaged for the seven surfaces. The relative standard deviation for SGM is less than 30%, except around $\theta_r = 0°$ where the calculated BRDF fluctuates due to the small solid angle ($\Delta\omega_r = \sin\theta_r \Delta\theta_r \Delta\phi_r$). Although the number of ray bundles in MSM can be increased to reduce numerical fluctuations,

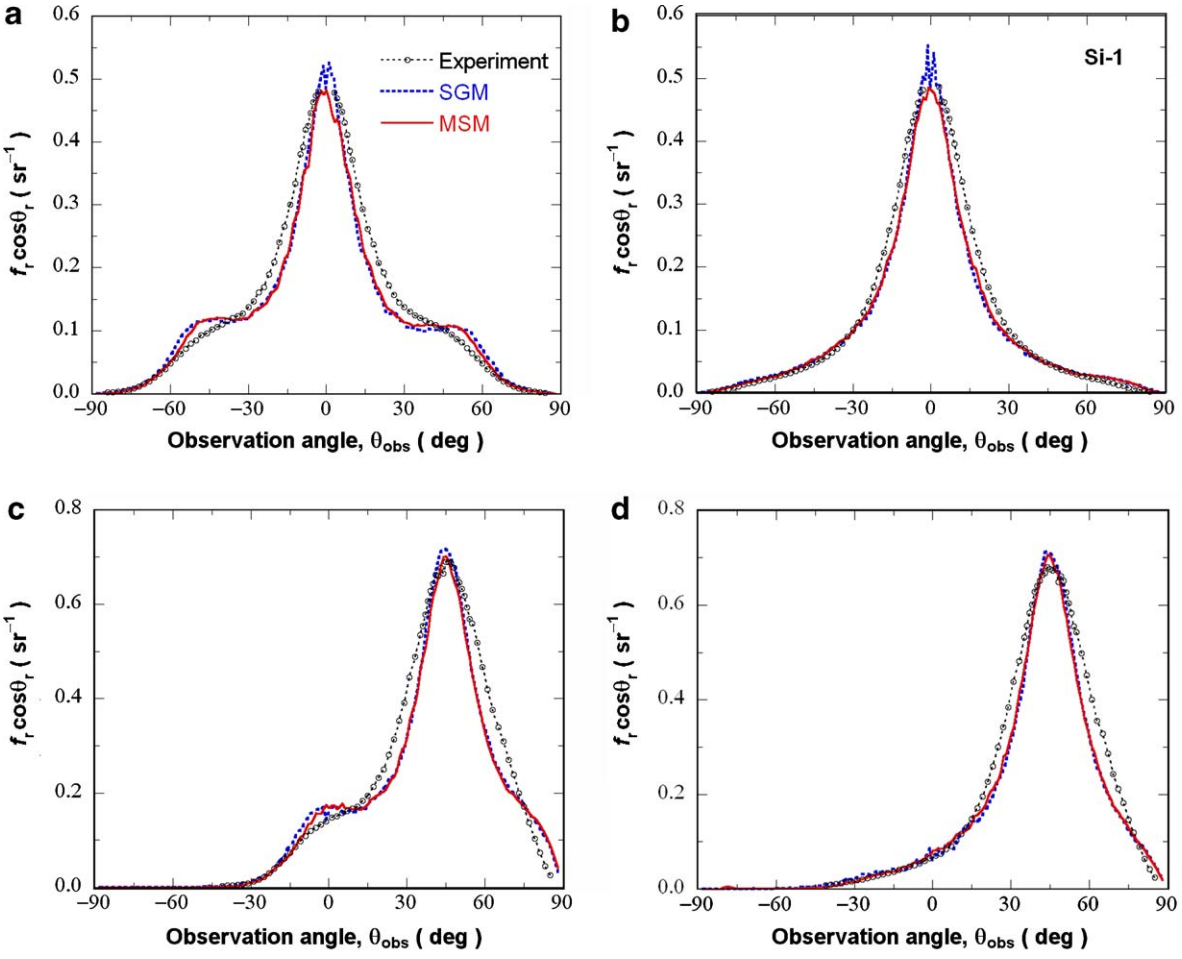

Fig. 3. Comparison of the in-plane BRDF of Si-1 for random polarization. (a) $\theta_i = 0°$ and $\phi_i = 0°$; (b) $\theta_i = 0°$ and $\phi_i = 45°$; (c) $\theta_i = 45°$ and $\phi_i = 0°$; (d) $\theta_i = 45°$ and $\phi_i = 45°$.

the number in SGM is limited to the number of topographic measurements, resulting in a larger standard deviation. It takes 20 min for SGM and 40 min for MSM to complete the calculation of each sample using a computer with a 3.2 GHz Pentium 4 processor and 2 GB memory. Although MSM is generally faster than SGM in calculation, the former takes more time than the latter due to the following reasons. The rejection method requires much more time for anisotropic surfaces than for Gaussian surfaces. The large difference between a weighted SDF and a comparison function increases the probability that a microfacet generated with uniform random numbers is rejected until another microfacet is accepted. The more microfacets that are rejected, the longer it takes to accept a microfacet that would follow the correct SDF of the surface [35]. It takes less time for MSM than for SGM to achieve the same standard deviation.

Predicted and measured in-plane BRDFs are compared first to verify the Monte Carlo ray-tracing algorithms. Note that the azimuthal angles ϕ_i and ϕ_r are measured from the x-axis in the counter-clockwise direction as shown in Fig. 1. When $\theta_i = 0°$, both the azimuthal angle of incidence ϕ_i and the plane of incidence become arbitrary. Nevertheless, if θ_i is treated as infinitesimal, ϕ_i can be defined even at $\theta_i = 0°$. Similarly, ϕ_r can be also defined when $\theta_r = 0°$. After the planes of incidence and reflection are identified, two linear polarizations of incidence and the in-plane BRDF ($\phi_r = \phi_i$ or $\phi_i + 180°$) are subsequently defined at $\theta_i = 0°$ and $\theta_r = 0°$. As mentioned earlier, depolarization does not occur for the in-plane BRDF with first-order scattering. The fourfold symmetry of the SDFs shown in Fig. 2 implies that the BRDF along the row ($\phi_i = 0°$) essentially equals to that along the column ($\phi_i = 90°$). The equality also holds for those along the two diagonals ($\phi_i = 45°$ and 135°). Calculated in-plane BRDFs for $\phi_i = 0°$ and 90° are averaged and indicated as $\phi_i = 0°$ for the row and column directions. Similarly, calculation results for $\phi_i = 45°$ and 135° are averaged and indicated as $\phi_i = 45°$ for the two diagonal directions.

The in-plane BRDFs of Si-1 for random polarization are shown in Fig. 3 for different values of θ_i and ϕ_i. Throughout this paper, the BRDF is presented in terms of $f_r \cos\theta_r$, which is proportional to the reflected energy. Here, the observation angle θ_{obs} is defined as θ_r when $\phi_r = \phi_i + 180°$ and $-\theta_r$ when $\phi_r = \phi_i$. Fig. 3 shows that SGM and MSM essentially yield the same results, which agree reasonably well with measurements for all the cases. The measured and predicted BRDFs agree well at the specular peak $\theta_{obs} = -45°$ for $\theta_i = 45°$. Because the BRDF within ±2.5° in the retro-reflection direction cannot be measured with the TAAS,

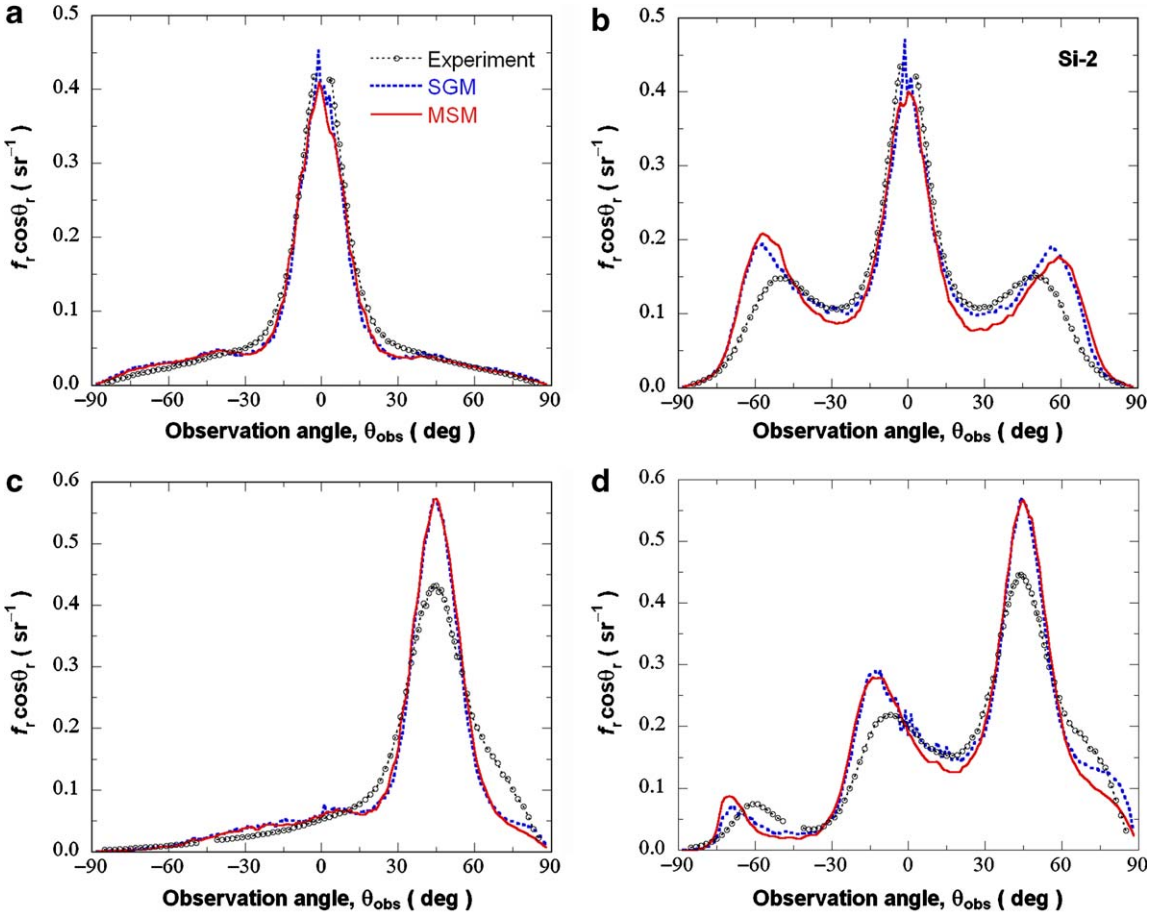

Fig. 4. In-plane BRDF of Si-2 for random polarization. (a) $\theta_i = 0°$ and $\phi_i = 0°$; (b) $\theta_i = 0°$ and $\phi_i = 45°$; (c) $\theta_i = 45°$ and $\phi_i = 0°$; (d) $\theta_i = 45°$ and $\phi_i = 45°$.

no data are available for $-2.5° < \theta_{obs} < 2.5°$ in Fig. 3a and b and for $-47.5° < \theta_{obs} < -42.5°$ in Fig. 3c and d. It is well-known that scattering in the retroreflection direction can be greatly enhanced [44]. Thus, any interpolation or extrapolation of the BRDF in this region is not acceptable. Numerical fluctuations of SGM appear around $\theta_{obs} = 0°$ due to the small solid angle. The predicted BRDF curves for $\phi_i = 0°$ as shown in Fig. 3a and c have much more distinct shoulders than the measured, which may be caused by the artifacts in the AFM measurements. It should be noted that the reproducibility of the BRDF measurements is very good [29]. Around the specular and retroreflection directions or at large θ_r, the effect of wave interference may be sufficient to invalidate the assumption of geometric optics. Therefore, the limitation of GOA may be responsible for the overprediction in Fig. 3c when $\theta_{obs} > 75°$.

Fig. 4 shows the same comparison for Si-2, which has larger σ and w and is more anisotropic than Si-1. In Fig. 4a, prediction and measurement agree well, except near $\theta_{obs} = 0°$, where the measurements within $\pm 2.5°$ could not be taken and the prediction has large fluctuations. While the Monte Carlo methods capture the general features and trends of the measured BRDF, relatively large discrepancies appear in other cases, especially when side peaks occur. When $\theta_i = 0°$ and $\phi_i = 45°$, the BRDF curves shown in Fig. 4b exhibit two large side peaks. These side peaks are associated with the side peaks in the SDF of Si-2 at $|\zeta_x| \approx |\zeta_y| \approx 0.36$; see Fig. 2b. The Monte Carlo methods also predict the side peaks in the BRDF, but they fail to predict their position and magnitude accurately. The predicted side peaks are located on the average at $\theta_r = 57°$ whereas the measured are at 50°. The inclination angle of microfacets is half of θ_r at $\theta_i = 0°$. Therefore, the measured side peaks in the BRDF correspond to an inclination angle of 25°, which is very close to the angle of 25.2° between any of the four {3 1 1} planes and the (100) plane. On the other hand, the predicted side peaks correspond to an inclination angle of 28.5°. This value is almost the same as that calculated from the average slope of $|\zeta_x| = |\zeta_y| = 0.38$ (28.0°), indicating consistency with the AFM measurements. Consequently, the position of the side peaks obtained from BRDF measurements is more reliable than that predicted by the Monte Carlo methods using the AFM measurements. Due to the artifacts in the AFM measurements, BRDF values are overpredicted when $50° < \theta_r < 80°$ and underpredicted when $15° < \theta_r < 50°$ (noticeably for MSM) in Fig. 4b.

When $\theta_i = 45°$ as shown in Fig. 4c and d, the two Monte Carlo methods noticeably overpredict BRDFs around the specular peak and underpredict at large observation angles. The overprediction is approximately 27%, presumably because the decrease in the optical roughness, defined as $\sigma \cos\theta_i/\lambda$, has invalidated the assumptions made in GOA [13,14]. The underprediction at $60° < \theta_{obs} < 85°$ may result from the artifacts in the AFM measurements and the limitation of GOA. In Fig. 4d, MSM yields smaller values at large θ_{obs} than SGM. Multiple scattering is usually significant at large reflection angles and causes the difference between SGM and MSM, which will be discussed later. When $\theta_i = 45°$ and $\phi_i = 45°$, a small side peak appears at $\theta_{obs} = -60°$ in the measured BRDF curve and at $\theta_{obs} = -71°$ in the predicted curves as shown in Fig. 4d. Zhu and Zhang [28] attributed the small side peak to microfacets having {1 1 1} orientation with an inclination angle of 54.7°. Accordingly, the small side peak should occur at $\theta_{obs} = -54.7 \times 2 + 45 = -64.4°$ if geometric optics is valid. The location of the small side peaks in the measured BRDF deviates from the predicted angles based on the crystalline orientation by 4.4°, which is significantly worse than the agreement for the large side peaks.

The effect of multiple scattering on the BRDF was investigated using SGM, which is more accurate since it does not employ the shadowing function. Only the results for Si-2 at $\theta_i = 45°$ and $\phi_i = 45°$ are shown in Fig. 5 for each polarization to illustrate the contribution of multiple scattering. The component of multiple scattering for s-polarization is discernable, albeit small. Due to the small contribution of multiple scattering for p-polarization, the component of multiple scattering in Fig. 5b is magnified

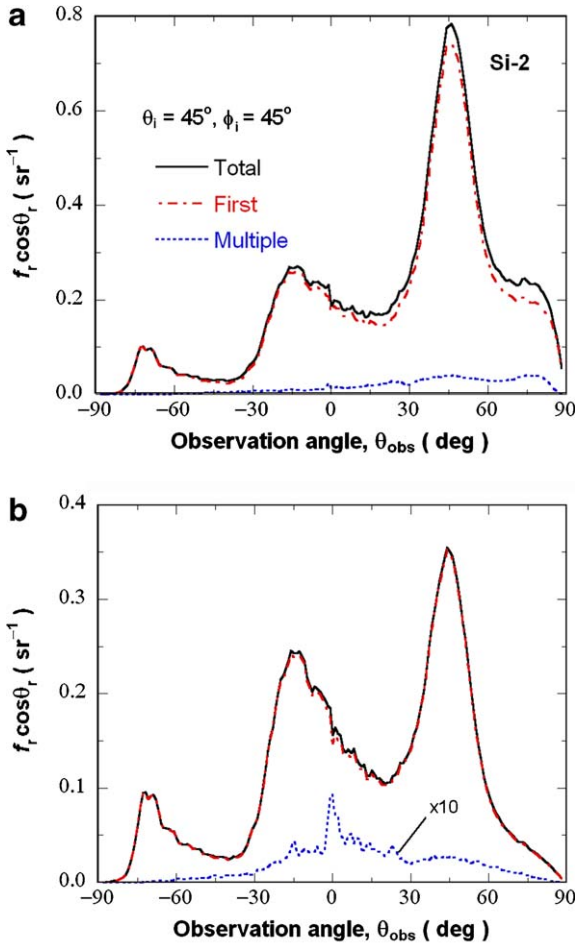

Fig. 5. Predicted first scattering and multiple scattering for the in-plane BRDF of Si-2 at $\theta_i = 45°$ and $\phi_i = 45°$. (a) s-polarization; (b) p-polarization, where the contribution of multiple scattering is magnified by a factor of 10 to make it clear.

by a factor of 10. As the local incidence angle increases, $\rho_{ss} = |r_s|^2$ monotonically increases, whereas $\rho_{pp} = |r_p|^2$ decreases to zero at the Brewster angle, which is 75.5° for silicon at 635 nm wavelength, and increases rapidly beyond the Brewster angle. If the reflectivity is small, the energy of ray bundles experiencing multiple scattering will be further reduced. Thus, multiple scattering is insignificant for p-polarization. The decrease of ρ_{pp} also explains why the specular peak for p-polarization is greatly reduced and becomes comparable to the large side peak, as seen from Fig. 5b. The contribution of multiple scattering to the directional-hemispherical reflectance is 6% for s-polarization and 3% for p-polarization, resulting in 4.5% for random polarization. The modeling also shows that the contribution of multiple scattering to the directional-hemispherical reflectance is less than 3% for Si-1 in the case of random polarization. This is consistent with the different slope distributions of Si-1 and Si-2. For the Au surfaces, on the other hand, multiple scattering contributes to the directional-hemispherical reflectance by less than 5% for Au-1 and by approximately 9% for Au-2, regardless of the polarization. This is because the reflectivity of gold is high and the difference between ρ_{ss} and ρ_{pp} is small.

The slight increase in multiple scattering at large θ_{obs}, as shown in Fig. 5, accounts for some of the disagreement between the BRDFs predicted by MSM and SGM as shown in Fig. 4. The disagreement between MSM and SGM is largely caused by the methods' differences in handling multiple scattering. The introduction of a shadowing function allows MSM to include re-striking to some extent, but it is not possible to fully account for the shadowing effect [22]. The Smith shadowing function takes the ratio σ/τ as an input. For Gaussian surfaces, the rms slope is related to the rms roughness and the autocorrelation length, $w = \sqrt{2}\sigma/\tau$. For the studied surfaces, however, w is not equal to $\sqrt{2}\sigma/\tau$, suggesting that the use of the shadowing function is only an approximation. In computation, $\sigma/\tau = 0.21$ is used as the input of the shadowing function because the use of w resulted in unacceptably large differences of the directional-hemispherical reflectance between the two methods. At $\theta_i = 45°$ and $\phi_i = 45°$, MSM predicted that multiple scattering contributes to the directional-hemispherical reflectance of Si-2 by 11% for s-polarization and 5% for p-polarization. For Au-2, MSM predicted that the contribution of multiple scattering to the directional-hemispherical reflectance is 16% for either polarization. The

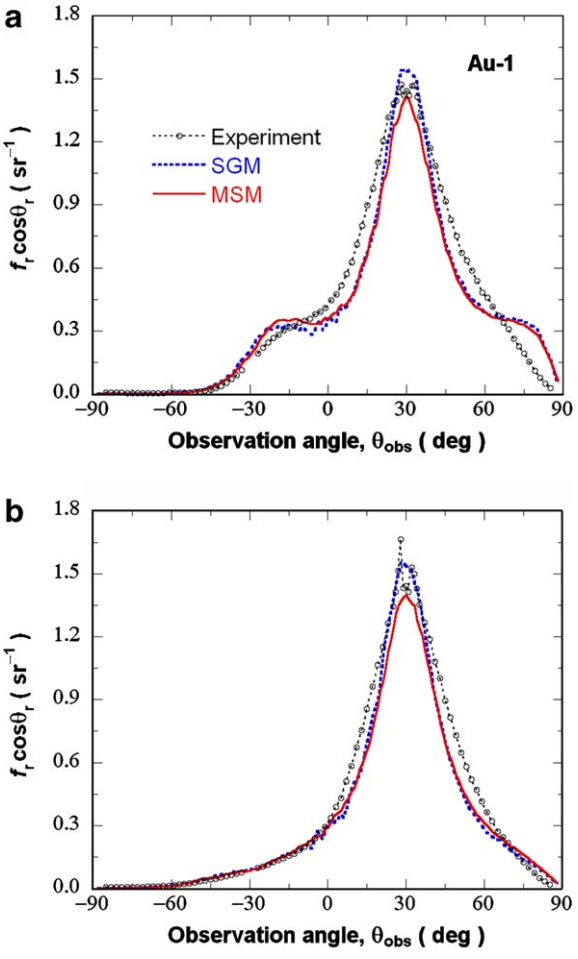

Fig. 6. Comparison of the in-plane BRDF of Au-1 at $\theta_i = 30°$ for random polarization. (a) $\phi_i = 0°$; (b) $\phi_i = 45°$.

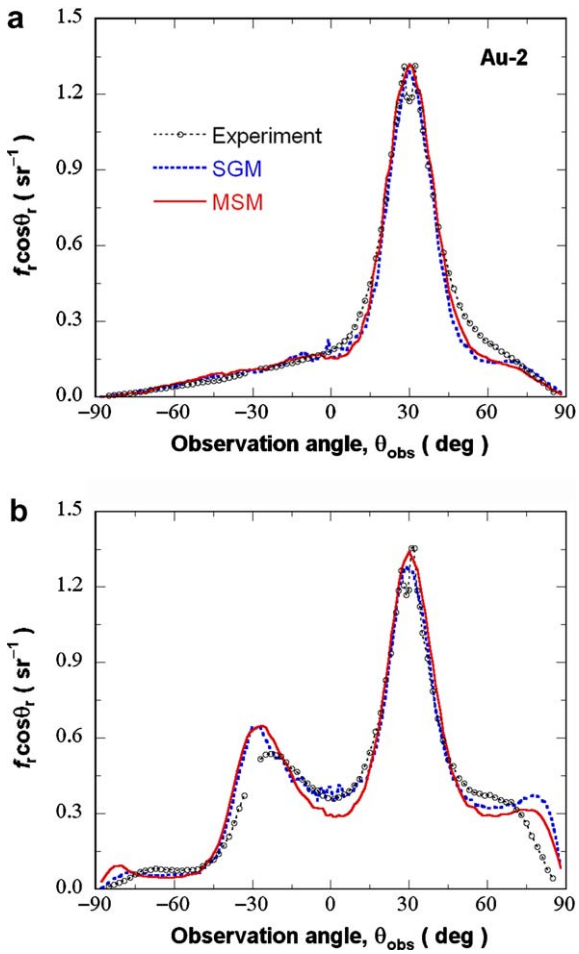

Fig. 7. In-plane BRDF of Au-2 at $\theta_i = 30°$ for random polarization. (a) $\phi_i = 0°$; (b) $\phi_i = 45°$.

shadowing function overpredicts multiple scattering and, subsequently, results in smaller BRDFs at large θ_{obs}.

The in-plane BRDFs of Au-1 for random polarization are presented in Fig. 6 at $\theta_i = 30°$ for two azimuthal incidence angles. The BRDF within $-27.5° < \theta_{obs} < -32.5°$ cannot be measured due to beam blocking. The same surface topographic data were used for BRDF calculations of Au-1 and Si-1. Because they possess the same roughness statistics, comparison shows similar trends for Au-1 and Si-1. However, the microfacet reflectivities of silicon and gold are 0.35 and 0.93 at normal incidence, respectively, and accordingly the BRDF of Au-1 is nearly three times that of Si-1. Furthermore, the measured BRDF curves exhibit two split peaks around the specular reflection $\theta_{obs} = 30°$, which is more distinct at $\phi_i = 45°$. Similar split peaks are observed for different values of θ_i including 45°. The Monte Carlo methods based on GOA do not predict the split peaks. Hence, wave interference may be important for highly reflecting surfaces. Future research is needed to study the effect of wave interference on gold-coated surfaces.

Fig. 7 shows the in-plane BRDF of Au-2. Measurements also display split peaks around the specular direction at both $\phi_i = 0°$ and $\phi_i = 45°$. The difference between prediction and measurement around the specular direction in Fig. 7 is smaller than that in Fig. 4c and d because the optical roughness is larger at $\theta_i = 30°$ than at $\theta_i = 45°$. The reflection angle corresponding to the small side peak is very large (around $\theta_{obs} = -80°$), and thus reflected rays are likely to re-strike another microfacet and be redirected. As a result, the small side peak is barely observed in experiment and SGM prediction. However, MSM overpredicts the small side peak in this case because of the difficulty in correctly modeling multiple scattering.

Fig. 8 shows the measured out-of-plane BRDFs of Si-2 at $\theta_i = 0°$ and $\phi_i = 45°$, along with those predicted by SGM. At this azimuthal angle of incidence, the in-plane BRDF is along $\phi_r = 45°$ and $\phi_r = 225°$. Because of the symmetry, the BRDF curves are only shown for ϕ_r from 0° and 45°. The BRDF depends little on ϕ_r when $\theta_r < 15°$, suggesting that the reflection is nearly isotropic at small θ_r. As θ_r increases, the dependence on ϕ_r increases and then decreases, becoming negligible at $\theta_r > 80°$. For $15° < \theta_r < 80°$, the BRDF increases with ϕ_r since the large side peak in the SDF is located along $\phi_r = 45°$. The BRDF for s-polarization is greater than that for p-polarization at $\phi_r = 45°$, and the difference decreases with reducing ϕ_r.

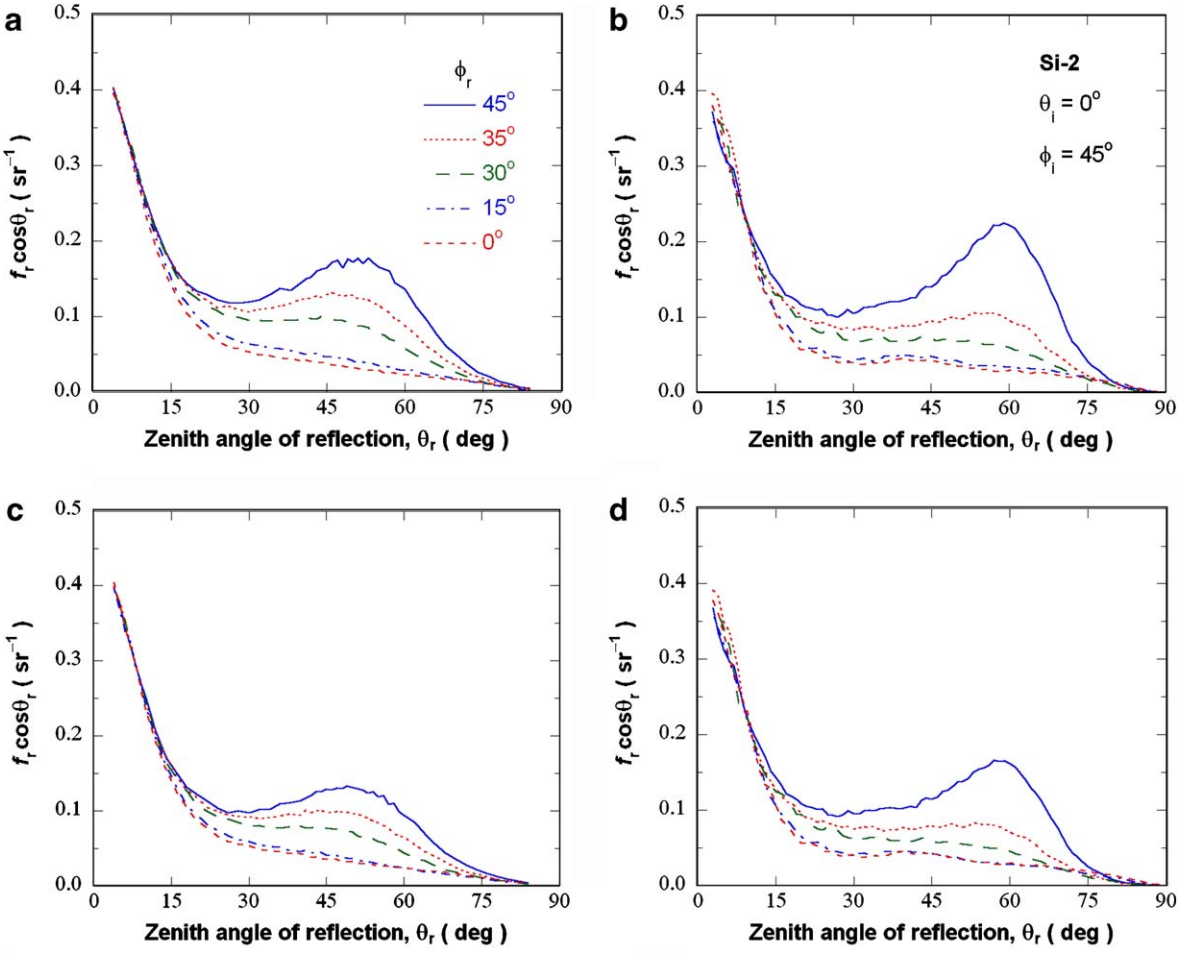

Fig. 8. Comparison of the out-of-plane BRDF of Si-2 at $\theta_i = 0°$ and $\phi_i = 45°$. (a) Experiment for s-polarization; (b) SGM calculation for s-polarization; (c) experiment for p-polarization; (d) SGM calculation for p-polarization.

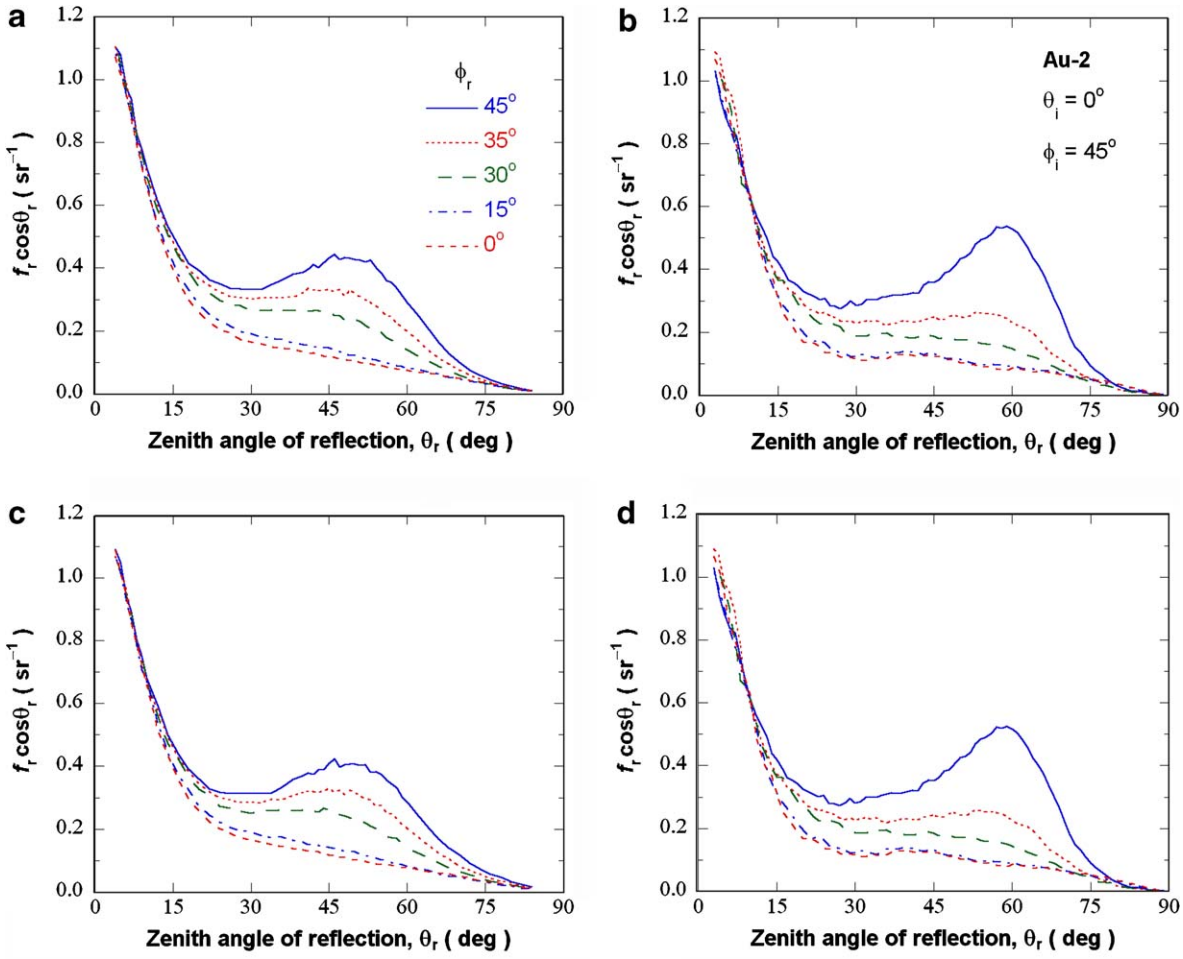

Fig. 9. Out-of-plane BRDF of Au-2 at $\theta_i = 0°$ and $\phi_i = 45°$. (a) Experiment for s-polarization; (b) SGM calculation for s-polarization; (c) experiment for p-polarization; (d) SGM calculation for p-polarization.

The BRDFs for the two polarizations are essentially the same at $\phi_r = 0°$. These trends can be understood by considering the microfacet reflectivities. For in-plane reflection ($\phi_r = 45°$), $\rho_{ss} = |r_s|^2$ and $\rho_{pp} = |r_p|^2$ while $\rho_{ps} = \rho_{sp} = 0$. From Eq. (5), $G_r = G_{r,s} + G_{r,p} = \rho_{ss}$ for s-polarization and $G_r = \rho_{pp}$ for p-polarization. This results in a larger BRDF for s-polarization than for p-polarization at $\phi_r = 45°$. For out-of-plane reflection ($\phi_i \neq \phi_r$), depolarization occurs and increases with $|\phi_i - \phi_r|$. For $\theta_i = 0°$ and $\phi_i = 45°$, it can be shown that $\mathbf{h}_r \cdot \mathbf{s}_i = 0$ and $\mathbf{h}_i \cdot \mathbf{s}_r = -\mathbf{v}_i \cdot \mathbf{s}_r$ at $\phi_r = 0°$. Substitution of these relations to Eq. (4) gives $\rho_{pp} = \rho_{sp} = |r_p|^2$ and $\rho_{ss} = \rho_{ps} = |r_s|^2$. Consequently, $G_r = |r_p|^2 + |r_s|^2$ becomes the same for either incident polarization. In other words, although the incidence is purely s- or p-polarized, it is evenly decomposed into s and p components in the local coordinates of the microfacet; thus, the BRDFs at $\phi_r = 0°$ are the same for both polarizations. The predicted BRDFs also indicate the same trend as the measured. Because the change of the polarization state is considered, the Monte Carlo methods can account for the dependence of BRDF on the polarization. Despite the good qualitative agreement, prediction shows notable disagreement with the experiment around the side peaks for $\phi_r = 45°$, similar to the observations made earlier with Fig. 4b.

The measured and predicted out-of-plane BRDFs of Au-2 are compared in Fig. 9 under the same conditions as those in Fig. 8. Because the same surface topographic data were used for Si-2 and Au-2, the features of scattering are very similar to those shown in Fig. 8 and will not be repeated. Compared to the results in Fig. 8, the large microfacet reflectivity of a gold film significantly increases the BRDF. Because the effect of polarization on the microfacet reflectivity of gold is not as significant as on that of silicon, the BRDFs for two polarizations differ only slightly.

The out-of-plane BRDFs of Au-1 and Au-2 predicted with MSM at $\theta_i = 30°$ are presented in Fig. 10 as contour plots in a polar coordinate system. MSM was chosen because it reduces numerical fluctuations with small standard deviations. In these plots, the radial and azimuthal coordinates, respectively, correspond to θ_r and ϕ_r, and the z-axis represents $f_r \cos\theta_r$. Because first-order scattering is dominant, all the BRDFs resemble the contour plot of SDFs in Fig. 2. The BRDFs depend little on ϕ_r around the specular direction, but the dependence becomes large as angular separation from the specular peak increases.

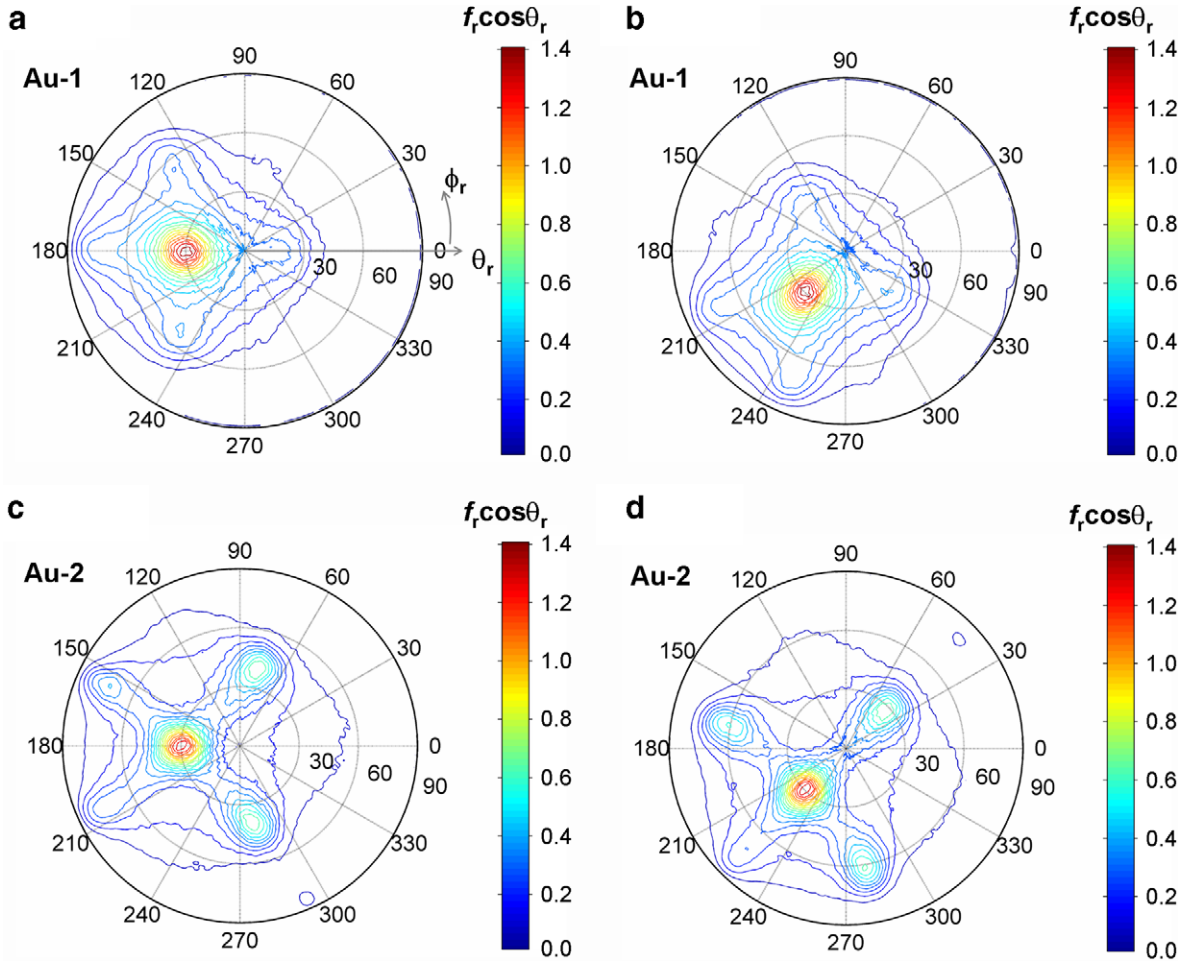

Fig. 10. BRDF predicted by MSM at $\theta_i = 30°$ for random polarization: (a) Au-1 at $\phi_i = 0°$; (b) Au-1 at $\phi_i = 45°$; (c) Au-2 at $\phi_i = 0°$; (d) Au-2 at $\phi_i = 45°$. In the polar contour plots, the radial coordinate corresponds to θ_r, and the azimuthal coordinate corresponds to ϕ_r.

The region where the BRDF is independent of ϕ_r is broader for Au-1 than for Au-2 because Au-1 is not as anisotropic as Au-2. The predicted BRDFs for Au-2 display a strong specular reflection peak along with the four large side peaks associated with {3 1 1} planes. In addition, a small side peak associated with a {1 1 1} plane appears at large θ_r in Fig. 10c at $\phi_r = 294°$ and another in Fig. 10d at $\phi_r = 45°$. The actual magnitude of the small side peaks may be smaller than that predicted by MSM, and their positions may shift towards a smaller θ_r. Nevertheless, Fig. 10 indicates that the Monte Carlo method is an effective technique to study the BRDF of surfaces with anisotropic roughness.

5. Conclusions

For the first time, the measured 2-D topographic data from an AFM are incorporated into the Monte Carlo ray-tracing methods to model the BRDF of dielectric and metallic surfaces whose roughness follows non-Gaussian and anisotropic statistics. The agreement between the model prediction and the experimental measurement demonstrates that the use of the measured surface topography is essential for modeling the BRDF of anisotropic surfaces. The consideration of the change of the polarization state is necessary to correctly model the out-of-plane BRDF. Surface characterization indicates that the gold and silicon surfaces are statistically the same, and thus their BRDFs describe many features in common. However, the occurrence of the split peaks in the specular direction only for gold surfaces implies that the effect of wave interference prevails more for gold surfaces than for silicon surfaces. The Monte Carlo method predicts that first-order scattering is dominant for both silicon and gold surfaces. Some differences between prediction and measurement are observed and mainly ascribed to the artifacts in the AFM measurement and the limitation of GOA. The versatile Monte Carlo modeling tools developed through the present study help gain a better understanding of the directional radiative properties of microrough surfaces and, furthermore, will have an impact on thermal metrology in the semiconductor industry.

Acknowledgements

This work was supported by the National Science Foundation (CTS-0236831). Valuable discussions with Prof.

Yiping Zhao, Dr. Qunzhi Zhu, Dr. Heungjoo Shin, and Mr. Joel Pikarsky are much appreciated.

References

[1] P.J. Timans, The thermal radiative properties of semiconductors, in: F. Roozeboom (Ed.), Advances in Rapid Thermal and Integrated Processing, Academic Publishers, Dordrecht, Netherlands, 1996, pp. 35–102.

[2] C. Schietinger, Wafer temperature measurement in RTP, in: F. Roozeboom (Ed.), Advances in Rapid Thermal and Integrated Processing, Academic Publishers, Dordrecht, Netherlands, 1996, pp. 103–123.

[3] Z.M. Zhang, Surface temperature measurement using optical techniques, in: C.L. Tien (Ed.), Annual Review of Heat Transfer, vol. 11, Begell House, New York, 2000, pp. 351–411.

[4] P. Vandenabeele, K. Maex, Influence of temperature and backside roughness on the emissivity of Si wafers during rapid thermal processing, J. Appl. Phys. 72 (12) (1992) 5867–5875.

[5] Y.H. Zhou, Y.J. Shen, Z.M. Zhang, B.K. Tsai, D.P. DeWitt, A Monte Carlo model for predicting the effective emissivity of the silicon wafer in rapid thermal processing furnaces, Int. J. Heat Mass Transfer 45 (9) (2002) 1945–1949.

[6] M.F. Modest, Radiative Heat Transfer, McGraw-Hill, New York, 1993 (Chapter 3).

[7] K. Masuda, T. Takashima, Y. Takayama, Emissivity of pure and sea waters for the model sea-surface in the infrared window regions, Remote Sens. Environ. 24 (2) (1988) 313–329.

[8] H.J. Lee, Q.Z. Zhu, Z.M. Zhang, Radiative properties of anisotropic microrough silicon surfaces, in: Proceedings of 38th AIAA Thermophysics Conference, 2005, AIAA-2005-5209.

[9] J.G. Burnell, J.V. Nicholas, D.R. White, Scattering model for rough oxidized metal surfaces applicable to radiation thermometry of reformer furnaces, Opt. Eng. 34 (6) (1995) 1749–1755.

[10] B. Adams, A. Hunter, M. Yam, B. Peuse, Determining the uncertainty of wafer temperature measurements induced by variations in the optical properties of common semiconductor materials, in: Proceedings of the 197th ECS Meeting, 2000 pp. 363–374.

[11] A.A. Maradudin, T. Michel, A.R. McGurn, E.R. Mendez, Enhanced backscattering of light from a random grating, Ann. Phys. 203 (2) (1990) 255–307.

[12] J.A. Sanchez-Gil, M. Nieto-Vesperinas, Light scattering from random rough dielectric surfaces, J. Opt. Soc. Am. A 8 (8) (1991) 1270–1286.

[13] P. Beckmann, A. Spizzichino, The Scattering of Electromagnetic Waves from Rough Surfaces, Artech House, Norwood, Massachusetts, 1987 (Chapter 5).

[14] J.A. Ogilvy, Theory of Wave Scattering from Random Rough Surfaces, Adam Hilger, Bristol, England, 1991 (Chapter 4).

[15] L. Tsang, J.A. Kong, Scattering of Electromagnetic Waves: Advanced Topics, Wiley, New York, 2001 (Chapter 2).

[16] K.E. Torrance, E.M. Sparrow, Theory for off-specular reflection from roughened surfaces, J. Opt. Soc. Am. 57 (9) (1967) 1105–1114.

[17] K. Tang, R.O. Buckius, A statistical model of wave scattering from random rough surfaces, Int. J. Heat Mass Transfer 44 (21) (2001) 4059–4073.

[18] L. Tsang, J.A. Kong, Energy conservation for reflectivity and transmissivity at a very rough surface, J. Appl. Phys. 51 (1) (1980) 673–680.

[19] J. Caron, J. Lafait, C. Andraud, Catastrophe theory interpretation of multiple peaks produced by light scattering from very rough dielectric surfaces, Physica B 325 (1–4) (2003) 76–85.

[20] C. Macaskill, Geometric optics and enhanced backscatter from very rough surfaces, J. Opt. Soc. Am. A 8 (1) (1991) 88–96.

[21] K. Tang, R.O. Buckius, The geometric optics approximation for reflection from two-dimensional random rough surfaces, Int. J. Heat Mass Transfer 41 (13) (1998) 2037–2047.

[22] Y.H. Zhou, Z.M. Zhang, Radiative properties of semitransparent silicon wafers with rough surfaces, J. Heat Transfer 125 (3) (2003) 462–470.

[23] H.J. Lee, B.J. Lee, Z.M. Zhang, Modeling the radiative properties of semitransparent wafers with rough surfaces and thin-film coatings, J. Quant. Spectrosc. Radiat. Transfer 93 (2005) 185–194.

[24] K. Yoshimori, K. Itoh, Y. Ichioka, Optical characteristics of a wind-roughened water surface: a two-dimensional theory, Appl. Opt. 34 (27) (1995) 6236–6247.

[25] A.P. Lyons, W.L.J. Fox, T. Hasiotis, E. Pouliquen, Characterization of the two-dimensional roughness of wave-rippled sea floors using digital photogrammetry, IEEE J. Oceanic Eng. 27 (3) (2002) 515–524.

[26] T. Karabacak, Y.-P. Zhao, T. Liew, G.-C. Wang, T.-M. Lu, Anisotropic scaling of hard disk surface structures, J. Appl. Phys. 88 (6) (2000) 3361–3366.

[27] Q.Z. Zhu, Z.M. Zhang, Anisotropic slope distribution and bidirectional reflectance of a rough silicon surface, J. Heat Transfer 126 (6) (2004) 985–993.

[28] Q.Z. Zhu, Z.M. Zhang, Correlation of angle-resolved light scattering with the microfacet orientation of rough silicon surfaces, Opt. Eng. 44 (7) (2005) 073601.

[29] Y.J. Shen, Q.Z. Zhu, Z.M. Zhang, A scatterometer for measuring the bidirectional reflectance and transmittance of semiconductor wafers with rough surfaces, Rev. Sci. Instrum. 74 (11) (2003) 4885–4892.

[30] Q.Z. Zhu, H.J. Lee, Z.M. Zhang, The validity of using thin-film optics in modeling the bidirectional reflectance of coated rough surfaces, J. Thermophys. Heat Transfer 19 (4) (2005) 548–557.

[31] S.C. Wu, M.F. Chen, A.K. Fung, Non-Gaussian surface generation, IEEE Trans. Geosci. Remote Sens. 26 (6) (1988) 885–888.

[32] E.I. Thorsos, The validity of the Kirchhoff approximation for rough surface scattering using a Gaussian roughness spectrum, J. Acoust. Soc. Am. 83 (1) (1988) 78–92.

[33] Y.-P. Zhao, G.-C. Wang, T.-M. Lu, Characterization of Amorphous and Crystalline Rough Surface: Principles and Applications, Academic Press, San Diego, California, 2001 (Chapter 2).

[34] M.E. Knotts, T.R. Michel, K.A. O'Donnell, Comparisons of theory and experiment in light scattering from a randomly rough surface, J. Opt. Soc. Am. A 10 (5) (1993) 928–941.

[35] W.H. Press, Numerical Recipes in C: The Art of Scientific Computing, second ed., Cambridge University Press, Cambridge, New York, 1992 (Chapter 7).

[36] B.G. Smith, Geometrical shadowing of a random rough surface, IEEE Trans. Antennas Propagation 15 (5) (1967) 668–671.

[37] B.K. Tsai, D.P. Dewitt, G.H. Shaffer, Macroscopic spread function analysis for subsurface scattering of semitransparent materials, J. Thermophys. Heat Transfer 8 (2) (1994) 202–207.

[38] J. Zaworski, J.R. Welty, B.J. Palmer, M.K. Drost, Comparison of experiment with Monte Carlo simulations on a reflective gap using a detailed surface properties model, J. Heat Transfer 118 (2) (1996) 388–393.

[39] J.R. Howell, The Monte Carlo method in radiative heat transfer, J. Heat Transfer 120 (3) (1998) 547–560.

[40] N.C. Bruce, Calculations of the Mueller matrix for scattering of light from two-dimensional surfaces, Waves Random Media 8 (1) (1998) 15–28.

[41] E.L. Church, P.Z. Takacs, Effects of non-vanishing tip size in mechanical profile measurements, in: C.P. Grover (Ed.), Proceedings of the Society of Photo-Optical Instrumentation Engineers, vol. 1332, 1991, pp. 504–514.

[42] K.A. O'Donnell, Effects of finite stylus width in surface-contact profilometry, Appl. Opt. 32 (25) (1993) 4922–4928.

[43] E.D. Palik, Handbook of Optical Constants of Solids, Academic Press, Orlando, Florida, 1985.

[44] K.A. O'Donnell, E.R. Mendez, Experimental study of scattering from characterized random surfaces, J. Opt. Soc. Am. A 4 (7) (1987) 1194–1205.